Geothermics 127 (2025) 103211

Contents lists available at ScienceDirect

Geothermics

journal homepage: www.elsevier.com/locate/geothermics

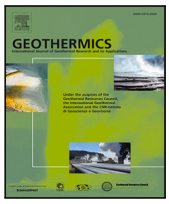

The seismic signature and geothermal potential of the Schwechat Depression in the Vienna Basin, Austria, from ambient noise tomography

C. Esteve [a,*], Y. Lu [a], J.M. Gosselin [b], R. Kramer [a], Y. Aiman [a], G. Bokelmann [a]

[a] Department of Meteorology and Geophysics, University of Vienna, Vienna, 1090, Austria
[b] Natural Resources Canada, Geological Survey of Canada - Pacific, Sidney, V8L 4B2, British Columbia, Canada

ARTICLE INFO

Keywords:
Ambient noise tomography
Seismic radial anisotropy
Geothermal exploration
Vienna basin

ABSTRACT

The Schwechat depression, in the Vienna Basin (VB) is currently the main target area for deep geothermal exploration in eastern Austria. Knowledge of the subsurface heavily relies on active seismic reflection profiling experiments that are expensive and logistically demanding. Affordable geophysical prospecting methods are needed to reduce subsurface uncertainty over large spatial areas. Over recent years, seismic ambient noise tomography (ANT) has proven to be a cost-effective and environment-friendly exploration technique fulfilling this need. Here, we present an ANT study of the central Vienna Basin revealing the shear-wave velocity, and shear-wave radial anisotropy structure down to 5 km beneath the surface. We deployed an array of 100 seismic nodal instruments during 5 weeks over summer 2023. We measured fundamental-mode Rayleigh and Love-wave group velocity dispersion from seismic noise correlations, and employed transdimensional Bayesian tomography to invert for isotropic Rayleigh and Love group velocity maps at periods ranging from 0.8 to 5.5 s. We then extracted Rayleigh and Love group velocity dispersion curves from the maps at all locations, and jointly inverted them for shear-wave velocity and radial anisotropy as a function of depth using a transdimensional Bayesian framework.

Our shear-wave velocity model reveals a basin-like low-velocity feature, interpreted as the seismic signature of the Schwechat depression. Another low-velocity feature is observed beneath the city of Vienna, which could be of great interest for geothermal exploration. The shear-wave velocity radial anisotropy structure indicates a thin negative anisotropy layer in the top 150 meters, likely associated with water-saturated open cracks. Between 150 meters and 1.5 km depth, we observe widespread positive radial anisotropy across the entire study area, corresponding to sub-horizontal layering within the Neogene basin. At greater depths, the Schwechat depression is characterized by positive radial anisotropy, while the edges of the Schwechat depression exhibit negative radial anisotropy due to steeply dipping strata and normal faults responsible for the formation of this major depocenter in the Vienna Basin.

1. Introduction

Austria aims to achieve carbon neutrality by 2040, and key strategies to attain this target involve substantial reductions in fossil fuel usage and the incorporation of renewable energy, notably geothermal energy. Developing geothermal resources is particularly relevant for district heating. Given that the highest geothermal heat flow occurs in the easternmost regions of Austria (Goetzl et al., 2010), encompassing the Vienna Basin (VB), urban centers in this area emerge as primary targets for exploration and potential development.

The geological evolution of the VB is a complex interplay of tectonic processes and sedimentary dynamics, reflecting its position at the convergence of the Eastern Alps, the Carpathians, and the Pannonian Basin. The basin's development initiated during the Miocene epoch, approximately 18 million years ago, as a result of extensional tectonics superimposed on the compressional regime of the Alpine orogeny (Lee and Wagreich, 2017). Due to changes in the local stress regime, a pull-apart geometry started to form (Hinsch et al., 2005), initiating large-scale sinistral strike-slip fault systems. These systems often originated from reactivated basement structures and were accompanied by significant normal faults with major offsets. This process resulted in intense segmentation of the basin into duplexes, where depocenters, such as the Schwechat depression, were filled with Neogene sediments up to 4000 meters thick (Elster et al., 2016). The tectonic activity during this phase was relatively subdued, but the region experienced significant isostatic adjustments and localized fault reactivation (Chwatal et al.,

* Corresponding author.
E-mail address: clement.esteve@univie.ac.at (C. Esteve).

https://doi.org/10.1016/j.geothermics.2024.103211
Received 21 August 2024; Received in revised form 13 November 2024; Accepted 24 November 2024
Available online 4 December 2024

2005). The basin's stratigraphy reveals a complex history of subsidence, sedimentation, and tectonic reactivation, which has largely shaped its current geothermal gradient and resource potential. This intricate geological history underscores the VB's significance as a natural laboratory for studying basin evolution, sedimentary processes, and geothermal energy development.

The VB has been extensively studied in the 20th century for oil and gas exploration and production (Rupprecht et al., 2018). In 2011, a test well called *Geotief1* was drilled (Fig. 1). This well was the initial deep geothermal exploratory well in Vienna and was drilled based on available geological and geophysical datasets. Although the goal was to reach the carbonate geothermal reservoir in the Alpine basement (Fig. 1), the target was not met. Following this, the situation was reassessed, making the Aderklaa Conglomerate formation in the Neogene basin the primary target, with the Triassic limestones and dolomites of the Alpine Calcareous basement as the secondary target. Recently, a large-scale (160 km^2) active 3-D seismic survey throughout the central Vienna Basin (north of the Danube River) was conducted to explore geothermal resources. The 3-D seismic survey was conducted in 2018–2019 by *OMV*. Unfortunately, there is no available information other than old 3D seismic reflection lines shared by *OMV* in the 2000s. The extent of the Aderklaa Conglomerate formation (with depths of around 3000 m and temperatures of up to 130 °C) in the Schwechat depression is the primary target geological layer for deep geothermal projects in the region, as it presents good geothermal potential and proximity to the heat distribution network infrastructure (Keglovic, 2023).

In the oil and gas industry, active seismic reflection surveys are a standard method for probing subsurface features up to a few kilometers deep. Nonetheless, the high cost and logistical challenges associated with these surveys can be impediments when applied to initial geothermal resource exploration and characterization. Unlike the oil and gas sector, the return on investment after seismic exploration is typically lower in the context of geothermal production, and the common proximity to urban areas may further complicate accessibility. Consequently, there is a distinct requirement for cost-effective and dependable alternatives to supplement traditional subsurface imaging for conducting focused surveys.

Ambient noise tomography (ANT) has been applied to imaging of volcanoes (e.g., Green et al., 2020), regional-scale lithospheric structure (e.g., Lu et al., 2018; Schutt et al., 2023), and regional imaging of sedimentary basins (e.g., Schippkus et al., 2018; Planès et al., 2019). Nodal seismic technology opens up new possibilities for applying noise-based methods at scales relevant to applications such as geothermal exploration. In recent years, noise-based passive seismic methods were successfully applied to large and dense seismic nodal arrays for obtaining detailed images of the subsurface, at the kilometer scale, in the context of geothermal exploration (Lehujeur et al., 2018; Cheng et al., 2021; Calò et al., 2023).

The nature of propagation of Rayleigh and Love surface waves allows for unique constraint on vertically and horizontally polarized shear-wave velocities, respectively. Combined, measurements of Rayleigh and Love dispersion enables for investigation of subsurface radial anisotropy. To date, only a limited number of studies have examined seismic radial anisotropy derived from Love and Rayleigh wave dispersion measurements at the geothermal reservoir scale (Tomar et al., 2016; Naghavi et al., 2019; Jiang and Denolle, 2022; Wu et al., 2024), and it has never been investigated in the Vienna Basin. Seismic radial anisotropy (ζ) arises from the difference between horizontally and vertically polarized shear-wave velocities, V_{S_H} and V_{S_V}, respectively. Several factors can influence seismic radial anisotropy in the crust, including the preferred alignments of open or water-filled cracks, foliations, shape-preferred orientation, and intrinsically anisotropic minerals (crystallographic preferred orientation; Crampin, 1981; Mainprice and Nicolas, 1989; Almqvist and Mainprice, 2017). Negative radial anisotropy ($V_{S_V} > V_{S_H}$) indicates a sub-vertical fabric, while positive radial anisotropy ($V_{S_H} > V_{S_V}$) signifies a sub-horizontal fabric (Dreiling et al., 2018). Jiang and Denolle (2022) determined the shear-wave radial anisotropy of the Kanto Basin in Japan, revealing strong negative radial anisotropy in the first 300 m likely associated with nearly-vertical open cracks in the subsurface. Below that, they observed positive radial anisotropy, interpreted to be controlled by horizontal sedimentary layering. Recently, Wu et al. (2024) presented the first shear-wave radial anisotropy model of the Hengill geothermal field in Iceland. Negative radial anisotropy dominates the top kilometer, reflecting the presence of vertical cracks, while deeper positive radial anisotropy is potentially explained by sub-horizontal lava deposits.

This study aims to ascertain the geological structure of the central Vienna Basin using ANT, with a specific focus on identifying velocity and radial anisotropy anomalies that may be associated with the local geothermal reservoir. The area is an ideal natural laboratory for testing ambient noise methods in a thick sedimentary basin, and comparing them with other conventional geophysical methods, particularly in the context of geothermal exploration.

2. Data and methods

2.1. Data

We deployed 44 nodes with an inter-station distance of ~ 200 m along the NW-SE trending profile across the central Vienna Basin (Fig. 1). Additionally, 58 nodes were deployed in an array with an inter-station distance of ~ 2 km around the profile. In total, the Eastern Vienna Array (EVA) consists of 102 seismic nodes. All seismic nodal instruments are FairfieldNodal Zland three-component (north, east, and vertical) nodes with a 5-Hz corner frequency. Each node recorded 40 days of continuous data. Two nodes (#165 and #168) suffered from battery issues, and were unusable for this study. The deployment of the whole array took 4 days with 2 2-person crews.

2.2. Surface-wave dispersion measurements

For each station, we pre-processed the continuous seismic data by detrending, band-pass filtering, glitch removal, and spectral whitening. Then, we stacked correlations of 2-min recording segments, with the causal and acausal sides folded to enhance the signal-to-noise ratio, over selected time periods. Our time period selection was based on two main considerations: enhancing far-field microseismic noise energy and minimizing interference from local noise sources within our target periods of interest. To that end, we analyzed the spectrum of noise recording, as shown for a representative station in Figure S1. We observed high noise energy in the microseismic band from approximately the 20th day until nearly the end of the deployment period (highlighted by the orange box in Fig. S1a and b), which defines the time interval selected for stacking in this study. This elevated noise level is likely originated from enhanced ocean activity (storm events). Although relatively high noise energy in the microseismic band is also present at the start of the deployment (indicated by the red box in Fig. S1a), the recordings are likely contaminated by wind-generated noise, especially in the horizontal components. Moreover, the wind-generated noise is amplified by local wind turbines, as evidenced by stronger noise levels at stations closer to the turbines. This process enabled the retrieval of clear Rayleigh and Love surface waves from the vertical–vertical and transverse–transverse components, respectively, covering periods from 0.5 to 6 s for approximately 3000 station pairs (Fig. S2). Then, we measured Rayleigh and Love group dispersion curves for each station pair with frequency re-centering (Shapiro and Singh, 1999), automated quality control, and visual inspection. Fig. 2 shows an example of dispersion analysis for the station-pair 152–186. Before the inversions, we removed dispersion measurements that had a propagation path length shorter than 1.5 wavelengths, and remove outliers with measured velocities outside of $\pm 2\sigma$ around the average group velocity at all periods considered in this study.

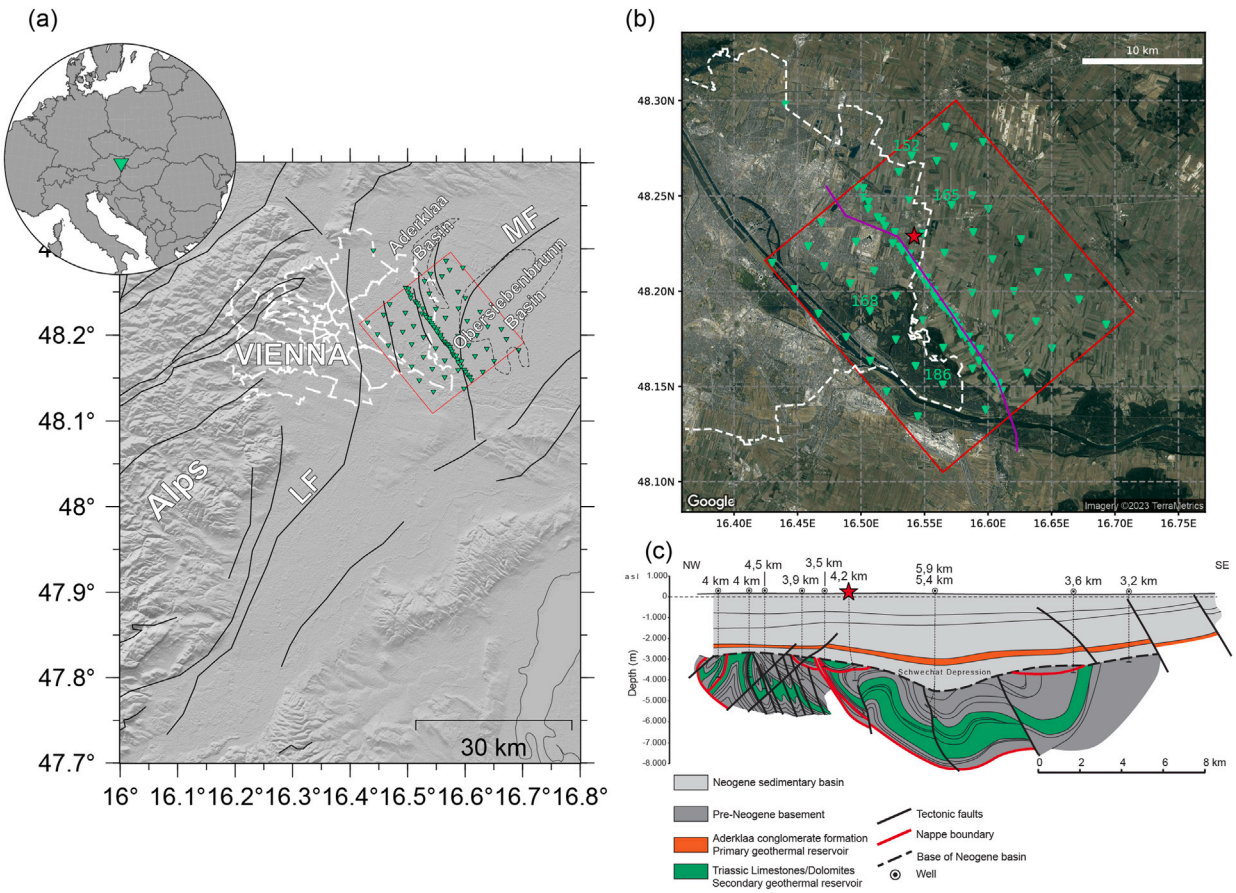

Fig. 1. (a) Topographic map of the central Vienna Basin region in Austria. Green inverted triangles depict the locations of EVA seismic nodes. The dashed black lines show the extent of known Pleistocene basins (Aderklaa and Obersiebenbrunn basins) from Salcher et al. (2012). The dashed white line shows the extent of the city of Vienna. Solid black lines show tectonic faults in and around the Vienna Basin. The purple line shows the location of the geological cross-section (c). Abbreviations: LF: Leopoldsdorf fault; MF: Markgrafneusiedl fault. (b) Zoom-in on the EVA station configuration. (c) Simplified geological profile across the central Vienna basin Elster et al. (modified from 2016). The red star shows the location of well *Geotief1*. (For interpretation of the references to color in this figure legend, the reader is referred to the web version of this article.)

2.3. 2D inversion procedure

We employed a Bayesian framework for the independent tomographic inversions of Rayleigh and Love wave group velocity dispersion measurements at 48 distinct periods ranging from 0.8 to 5.5 s. The objective is to determine group velocity maps along with their associated uncertainties. In this study, we modified the transdimensional tomography method of Gosselin et al. (2021), by allowing only the determination of isotropic group velocity.

Our approach for measuring Rayleigh and Love wave dispersion data does not allow us to quantify the uncertainty associated to these measurements. However, errors on surface wave travel times are considered unknown and are solved for as part of the inversion procedure. Errors on surface wave travel times are defined by:

$$\sigma_i = a\Delta_i + b \tag{1}$$

where Δ_i is the station-to-station distance for path i, and a and b are two unknown hyper-parameters that are solved for (Bodin et al., 2012). Prior information for a and b are given in Table S1. Uncertainties in the 2D group velocity maps will also include theory errors due to our assumption of straight ray wave propagation.

The group velocity maps are defined by a distribution of nodes. Each node, in addition to its spatial coordinates, is characterized by an isotropic velocity (i.e., either Rayleigh or Love group velocity). The inversion process determines both the number of nodes and their arrangement. Thus, the inversion is termed transdimensional, signifying that the model dimension is flexible. This flexibility proves advantageous, as areas of the model requiring increased complexity are represented by a greater number of nodes. In order to define group velocity over the entire map area, linear interpolation of group velocity between nodes is implemented within a Delaunay triangulation of the nodes (Hawkins et al., 2019). This parameterization scheme is applied across a regular (underlying) integration grid with a 500 m spacing during forward calculations (i.e., travel-time predictions).

The tomographic inversions conducted at each period are embedded within a Bayesian (probabilistic) framework to rigorously quantify uncertainties in the group velocity maps. The reversible-jump Markov-chain Monte Carlo (rjMcMC) method is employed to produce an extensive ensemble of samples (80 million), approximating the posterior probability density (PPD) of the model parameters (Green, 1995). In defining the model parameters, we establish broad, bounded, uniform prior distributions, facilitating a data-driven solution (Table S1). Random initial models are selected from the prior for 20 interacting, rjMcMC sampling chains. Each chain generates 4 million samples, with the initial 2 million discarded as burn-in samples, as they exhibit higher dependency on the initial random model. The mean and standard deviation of the remaining ensemble of models are computed at each location on the map, providing a representative model along with its associated uncertainty.

3. Group velocity maps

3.1. Synthetic resolution tests

To evaluate the resolution of our Rayleigh and Love group velocity models, we conducted synthetic checkerboard resolution tests with 2

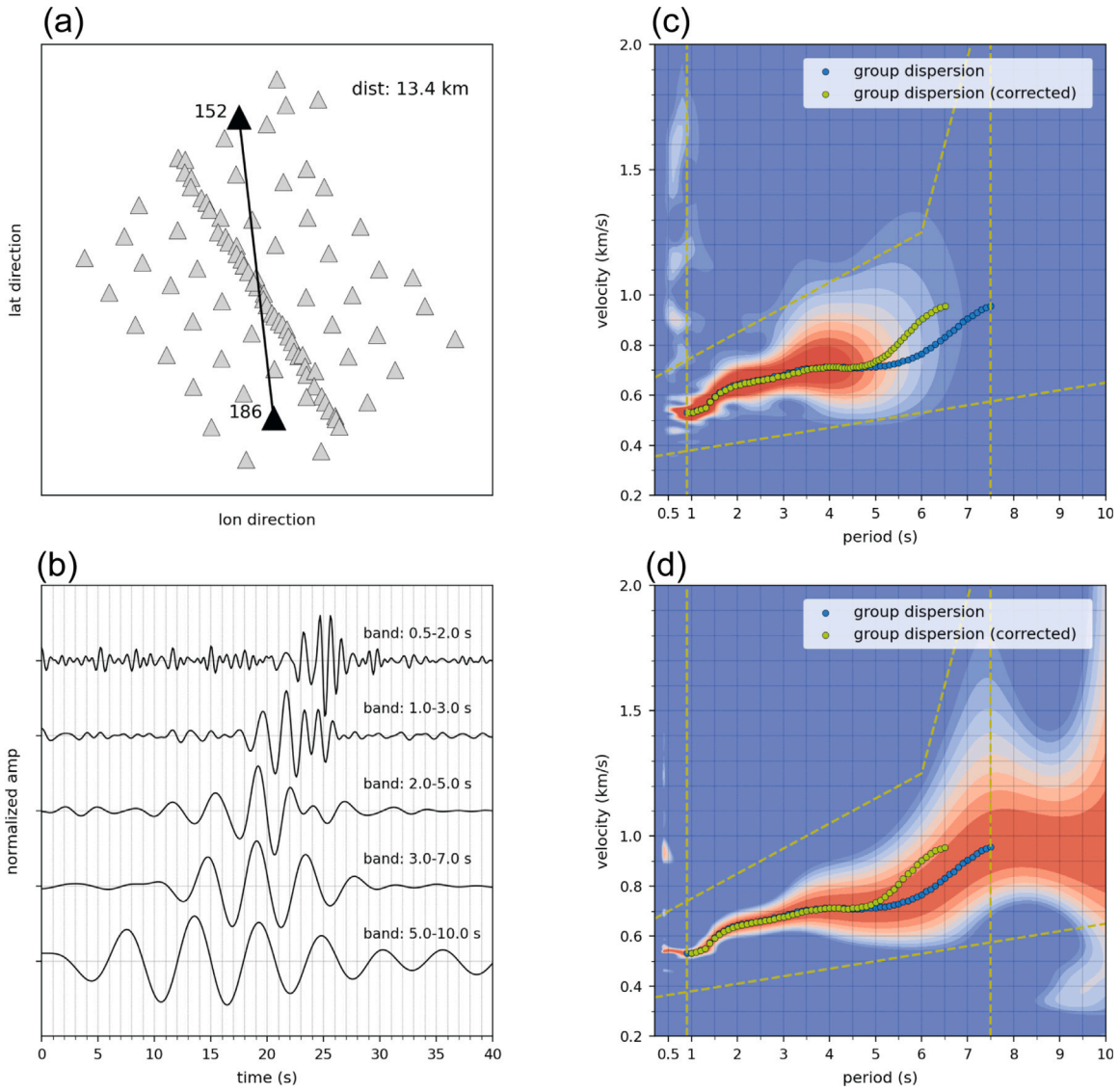

Fig. 2. Dispersion analysis for station-pair 152–186. (a) Map showing the seismic nodal network in gray and the station-pair 152–186 (highlighted in black, inter-station distance is 13.4 km). (b) Cross-correlations at different period bandwidths. Note the clear surface wave. Dispersion analysis for station pair 152–186 normalized by the maximum energy of the signal (c) and normalized at each frequency (d). Note the clear Love wave dispersion curve for periods ranging from 1 to 7.5 s. The green and blue dots show the picked dispersion curves with and without re-centering applied (*i.e., correction*), respectively. (For interpretation of the references to color in this figure legend, the reader is referred to the web version of this article.)

and 3 km anomaly sizes at periods of 2, 3 and 4 s. These tests comprised alternating patterns of slow and fast group velocity anomalies (±15% relative to the background mean velocity) for path coverage equivalent to our dataset at a period of 2 s (Figs. S3–S6). Gaussian-distributed errors with a standard deviation of 0.1 s were added to the simulated travel-time data. Using the same path coverage and model parameterization as the original tomography, we inverted these data to evaluate the recovery of the test model and infer resolution features.

These tests reveal the isotropic structure expected to be resolved for varying spatial extents of structures, considering data at periods of 2, 3 and 4 s. Similar patterns are anticipated in tests at other periods, with minor variations reflecting variability in inter-frequency path coverage. Overall, the recovery of input isotropic group velocity anomaly shapes and sizes is robust where path coverage density is high (Figs. S3–S6). The results suggest good recovery of isotropic group velocity structures with a lateral extent greater than or equal to 2 km throughout the central part of the study area.

3.2. Group velocity structure

Fig. 3 shows the mean isotropic Love and Rayleigh group velocity maps (Fig. 3, a-b-c-d) and associated errors obtained from the standard deviation from the rjMcMC samples (Fig. 3, e-f-g-h) at periods of 1 and 2 s across the central Vienna Basin. Group velocity maps at other periods are presented in the supplemental material (Figs. S7 and S8). The inversion considered absolute group velocities. The color ranges in Fig. 3 are selected as +/− 15% around the mean velocity of the model. This range does not represent the prior range of the model parameters, which is less informative. The Love and Rayleigh wave group velocities are extremely slow through the central Vienna Basin. For example, at a period of 5.5 s, Love and Rayleigh wave group velocities are on average slower than 1 km/s.

The Love group velocity maps reveal 3 distinct low velocity regions across the study area (labeled L1, L2 and L3). L1 underlies the eastern part of the city of Vienna at periods ranging from 0.8 to 3 s. L2 is located beneath the Aderklaa basin and can be observed at periods of

0.8 to 2 s. L3 is located directly to the east of the Markgrafneusiedl fault in the central Vienna basin and underlies the Obersiebenbrunn basin. The northern and southern areas exhibit higher velocities at all periods. Interestingly, we observe a sharp velocity contrast directly beneath the surface expression of the Markgrafneusiedl fault.

The Rayleigh group velocity maps differ notably from the Love wave maps. Using the average 1D V_S model derived in this study, we calculated sensitivity kernels for both Rayleigh and Love waves (Fig. S9), finding that they also vary at the same period. Overall, Love waves are more sensitive to the shallow structure, whereas Rayleigh waves exhibit depth sensitivity across a broader range. Consequently, we interpret the differences between Rayleigh and Love group velocity maps as characterizing vertical heterogeneity and material anisotropy.

The Rayleigh group velocity maps also reveal the presence of L1 at periods between 0.8 to 1.5 s, however L2 and L3 are not clearly defined. At periods $\leq$ 3 s, the southern and central regions display higher Rayleigh group velocities compared to the northern part. At 4 s, there is a high-velocity area located under the southern end of the profile. Then, a broad low-velocity area spans most of the southern region at periods $\geq$ 4.5 s (Fig. S8).

4. Shear-wave velocity structure

4.1. 1-D V_{S_V} depth inversion

The seismic velocity anomalies observed in the 2-D Love/Rayleigh group velocity maps cannot be directly associated with a specific depth (Fig. S9). As a result, a second inversion is required to obtain the 3-D V_{S_V} model and accurately identify these anomalies at depth. In the following sections, we present results in terms of V_{S_V} instead of V_{S_H} because the Rayleigh waves exhibit depth sensitivity to a broader range compared to Love waves. Recall that the 2-D Love/Rayleigh group velocity maps are defined on a regular (underlying) integration grid with a 500 m spacing used for surface-wave travel-time calculations. For each location in the underlying grid, we extract the tomographic results, including uncertainties, for both Rayleigh and Love group velocities at all periods. Joint inversions of Rayleigh and Love dispersion curves are performed independently for each grid location, the results of which are combined to form a pseudo-3-D model of shear-wave velocity and radial anisotropy. For the 1-D inversion at each grid location, the model is defined by a sequence of homogeneous layers. Each layer is defined by a value for depth, V_{S_V}, as well as a parameter ζ characterizing radial anisotropy as:

$$\zeta = 2\frac{(V_{S_H} - V_{S_V})}{(V_{S_H} + V_{S_V})}. \quad (2)$$

The inversion process determines both the number of layers in the 1-D model, as well as their arrangement. Similar to the tomographic inversions, the 1-D inversions are termed transdimensional, signifying that the model dimension is flexible such that depth ranges where the data require increased complexity are represented by a greater number of layers. For each grid location, the rjMcMC method is employed to produce an ensemble of samples (500,000) that approximate the posterior probability density (PPD) of the model parameters (Green, 1995). The group velocity map uncertainties extracted from the tomographic inversions are used as data errors when calculating model likelihood (i.e., misfit) in the 1-D inversions, thereby propagating uncertainties through both inversion steps of the overall ANT procedure. We establish relatively broad, bounded, uniform prior distributions between ±20% for ζ as a function of depth. For V_{S_V}, we establish a bounded, uniform prior distribution centered on a simple smooth V_{S_V} profile (Fig. S10), which is derived from the grid-search algorithm proposed by Lu et al. (2018). The width of the prior distribution about this simple 1-D profile varies from ±50% at the surface, to ±20% at a depth of 5 km. For each 1-D inversion, a random initial model was selected from the prior. The initial 100,000 models in the ensemble were discarded as burn-in samples, as they exhibit higher dependency on the initial random model. The mean and standard deviation of the remaining ensemble of 1-D models are computed, then combined. This provides a representative 3-D model of shear-wave velocity and radial anisotropy, along with their associated uncertainties.

Fig. 4 illustrates the results for a 1-D inversion. Specifically, Figs. 4a and 4b show the probabilities of V_{S_V} and radial anisotropy as functions of depth, respectively. Here, blue and yellow represent low and high probabilities, respectively. Note that probabilities are normalized at every depth, for visualization purposes. As the 1-D models are defined by a discrete set of homogeneous layers, the boundaries between these layers may represent physical geologic/stratigraphic boundaries. The probability that a layer boundary (interface) exists at a given depth can be determined from the ensemble of rjMcMC model samples. An example is shown in Fig. 4c. Lastly, the transdimensional nature of the inversion procedure is illustrated in Fig. 4d, which shows the distribution of the number of layers for the models in the ensemble of rjMcMC samples. In this example, the inversion favors approximately 9 layers.

4.2. 3-D V_{S_V} model

We present depth slices and profiles through the 3-D V_{S_V} model from the surface to 5 km depth (Fig. 5, 6 and S11). The depth slices show relative variations ($\delta V_{S_V} = \pm 15\%$) compared to the background mean velocity at each depth, which may enhance the apparent velocity contrasts (Fig. 5). In the vertical views, the V_{S_V} structure suggests a relatively uniform, layered medium with no major lateral velocity contrasts from the surface down to 1–1.5 km (Fig. 6). Pronounced velocity contrasts are observed only at depths greater than 1–1.5 km. We also present associated V_{S_V} uncertainties obtained from the rjMcMC samples (Fig. S12).

First, V_{S_V} are extremely slow in the central Vienna Basin ranging between 0.5 to 2.0 km/s from the surface to 5 km depth. We also note that the subsurface V_{S_V} structure is characterized by several velocity anomalies. Similar to the group velocity maps, three low-velocity areas (labeled L1, L2 and L3, Fig. 5) are present from the surface to 100 m depth. At greater depths, the southwestern region of the study area displays a significant low-velocity feature (labeled L4, Fig. 5), which narrows with increasing depth and extends in a northeast-southwest direction. We also observe high-velocity features on both sides of this low-velocity feature. At 4 km depth, we observe a low-velocity area to the east of the dense line of seismic nodes. Vertical profiles reveal a basin-like geometry for L4, as evidenced by the southeastward deepening of the 1.6 km/s V_{S_V} iso-velocity contour (Fig. 6). This basin-like structure gradually fades toward the northeast (Fig. 6; EE', FF') and is absent at shallower depths (surface to 1 km). Additionally, a smaller basin-like low-velocity region (labeled L1) extends to a depth of 4.5 km beneath eastern Vienna (Fig. 6), though it is less extensive than L4. To the northeast of the study area, a relatively faster feature is present at depths ranging between 1.5 and 3 km depth (Fig. 6; profiles EE' and FF').

The high V_{S_V} uncertainties correlate with layer interfaces at depth (Fig. 6). At these depths, the figure illustrates how model uncertainty is characterized by both the uncertainty in V_{S_V} of individual layers as well as the uncertainties in interface depths. We observe two main layer interfaces: one between 1 and 2 km depth and another between 3 and 4 km depth. We also note that the deeper interface is less distinct than the shallow one, likely due to poorer constraints.

4.3. Radial anisotropy

Figs. 7, 8 and S13 show the mean values of radial anisotropy and associated uncertainties obtained from the ensemble of rjMcMC samples, respectively. The radial anisotropy indicates the difference

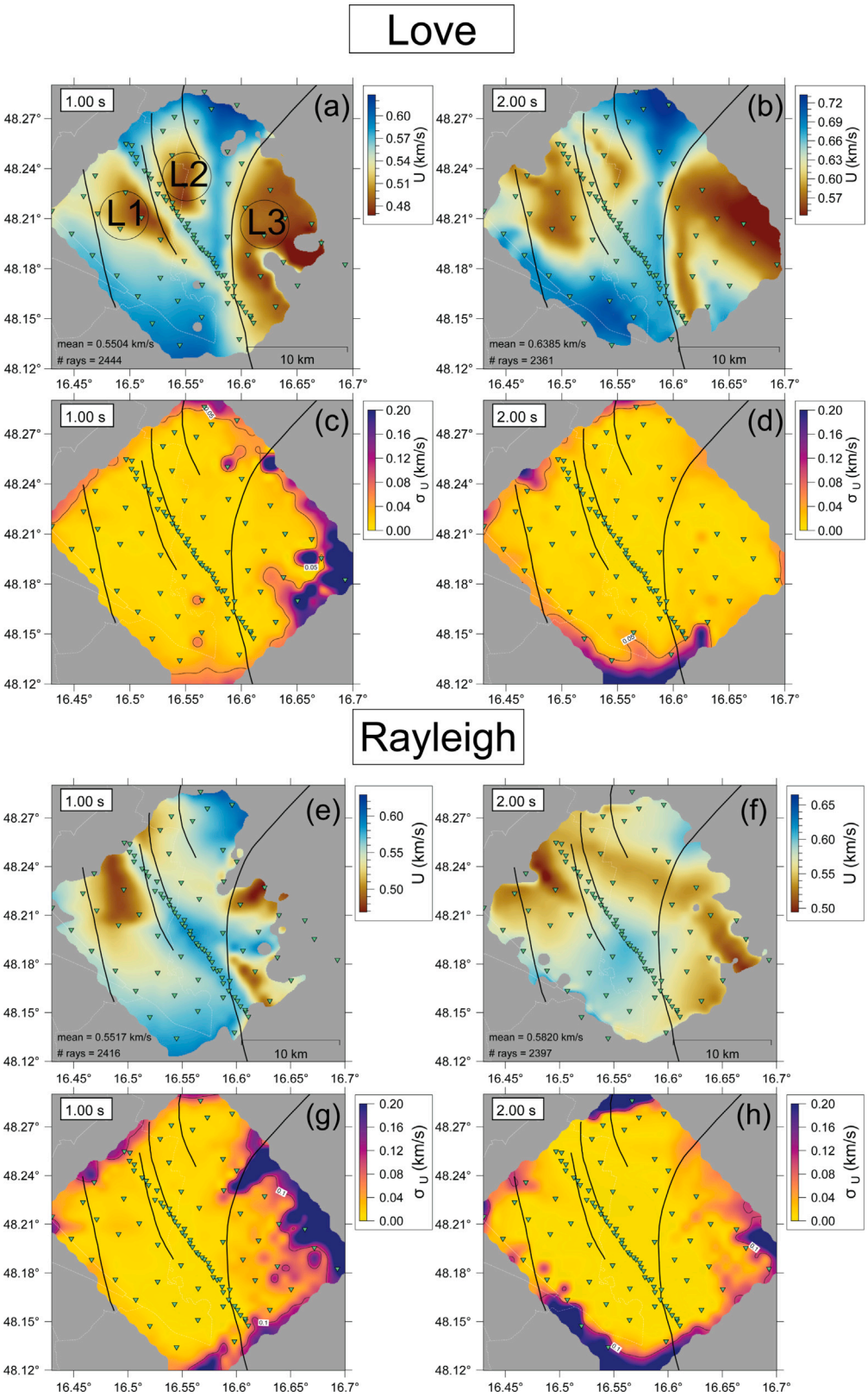

Fig. 3. Mean fundamental-mode Love (a-b-c-d) and Rayleigh wave (e-f-g-h) group velocities at 1 and 2 s periods and associated standard deviations obtained from the ensemble of rjMcMC samples. Areas with a standard deviation higher than 0.05 km/s are masked in gray color.

between the velocities of the vertically polarized S-wave (V_{S_V}) and the horizontally polarized S-wave (V_{S_H}) (Almqvist and Mainprice, 2017).

Our model displays several radial anisotropy anomalies between the surface and 4 km depth across the study area. First, we observe a widespread negative radial anisotropy anomaly (labeled A, $V_{S_V} > V_{S_H}$) from the surface to approximately 150 m depth (Fig. 7, 8) and, then, a positive radial anisotropy anomaly from 0.15 km to 1.20 km depth (labeled B, $V_{S_H} > V_{S_V}$). Between 1.5 km and 3 km depth, a negative

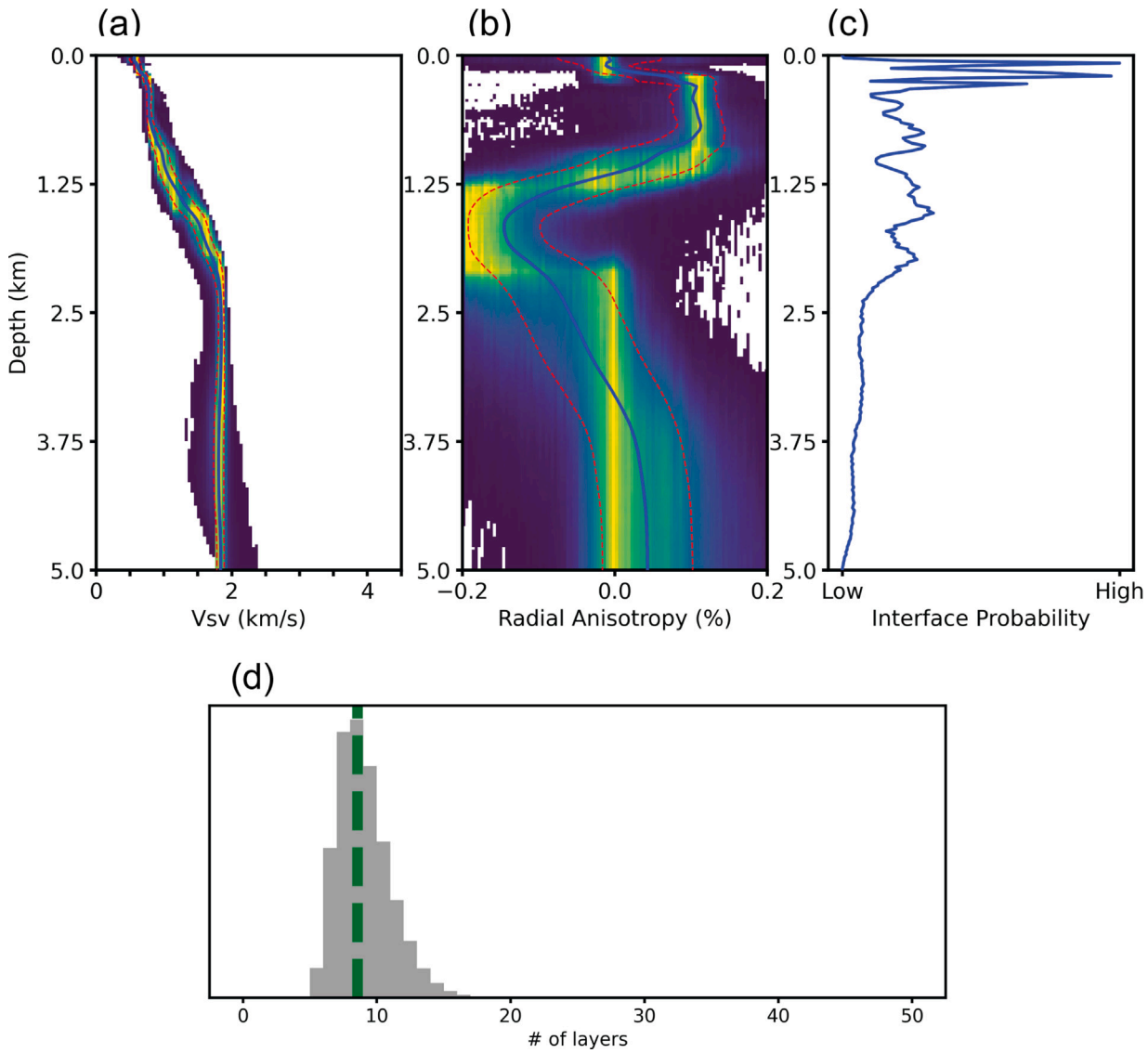

Fig. 4. (a) Probability profiles for V_{S_V}. The solid blue line shows the mean V_{S_V} profile and red dashed-line shows the standard deviation. (b) Probability profiles for the radial anisotropy. The solid blue line shows the mean radial anisotropy profile and red dashed-line shows the standard deviation. (c) Probability of a discontinuity as a function of depth. (d) histogram of the posterior distribution on the number of layers. Green dashed-line shows the average number of layers. (For interpretation of the references to color in this figure legend, the reader is referred to the web version of this article.)

radial anisotropy anomaly is located beneath eastern Vienna and to the East ($\zeta < 10\%$, labeled C). The southeasternmost part of the city of Vienna is underlain by a positive radial anisotropy anomaly ($\zeta > 10\%$, labeled D).

Along profile AA', we identify three radial anisotropy anomalies (labeled A, B, and C) between the surface and a depth of 3 km (Fig. 8). Along profile BB', positive and negative radial anisotropy anomalies (labeled B and C, respectively) are observed within the same depth range (approximately 1.5 to 3 km), positioned next to each other. Along profile CC', the positive radial anisotropy anomaly (labeled D) is slightly deeper compared to profile BB' and a thin negative radial anisotropy is noted between anomalies labeled B and D. Along profiles DD', EE', and FF', the positive radial anisotropy anomaly (labeled D) appears segmented and damped ($\zeta > 5\%$) and is located further north on profile FF'. Lastly, the negative radial anisotropy anomaly (labeled C) becomes thicker from profile CC' to profile FF' (Fig. 8).

The uncertainties in shear-wave radial anisotropy align with layer interfaces in a way similar to the V_{S_V} uncertainties (Fig. 8). Between depths of 1 to 2 km and 3 to 4 km, high uncertainties reflect the presence of a layer interface. At greater depths, while layer interfaces remain still present, they become less pronounced compared to those at shallower levels. This highlights the differences in sensitivities of both datasets with respect to depth in the subsurface, where the Love wave data set is less sensitive at greater depths (Fig. S9).

5. Discussion

5.1. Near-surface V_{S_V} structure

Our V_{S_V} model reveals significant heterogeneity in the near-surface V_{S_V} structure beneath the central Vienna Basin (Fig. 5). Similar to the 2D group velocity maps, a series of low V_{S_V} zones extend from the surface to a depth of 100 m. In particular, the slowest V_{S_V} values (labeled L3) are detected immediately east of the Markgrafneusiedl fault (MF), aligning with the modeled thickness of Pleistocene sediments (Beidinger et al., 2011) and corresponding to the Obersiebenbrunn sub-basin. Similarly, the low-velocity area (labeled L2) corresponds to the location of the Aderklaa Pleistocene sub-basin Salcher et al. (Fig. 1, 2012). These basins consist of unconsolidated, loose fluvial sediment deposits, forming grabens along reactivated major

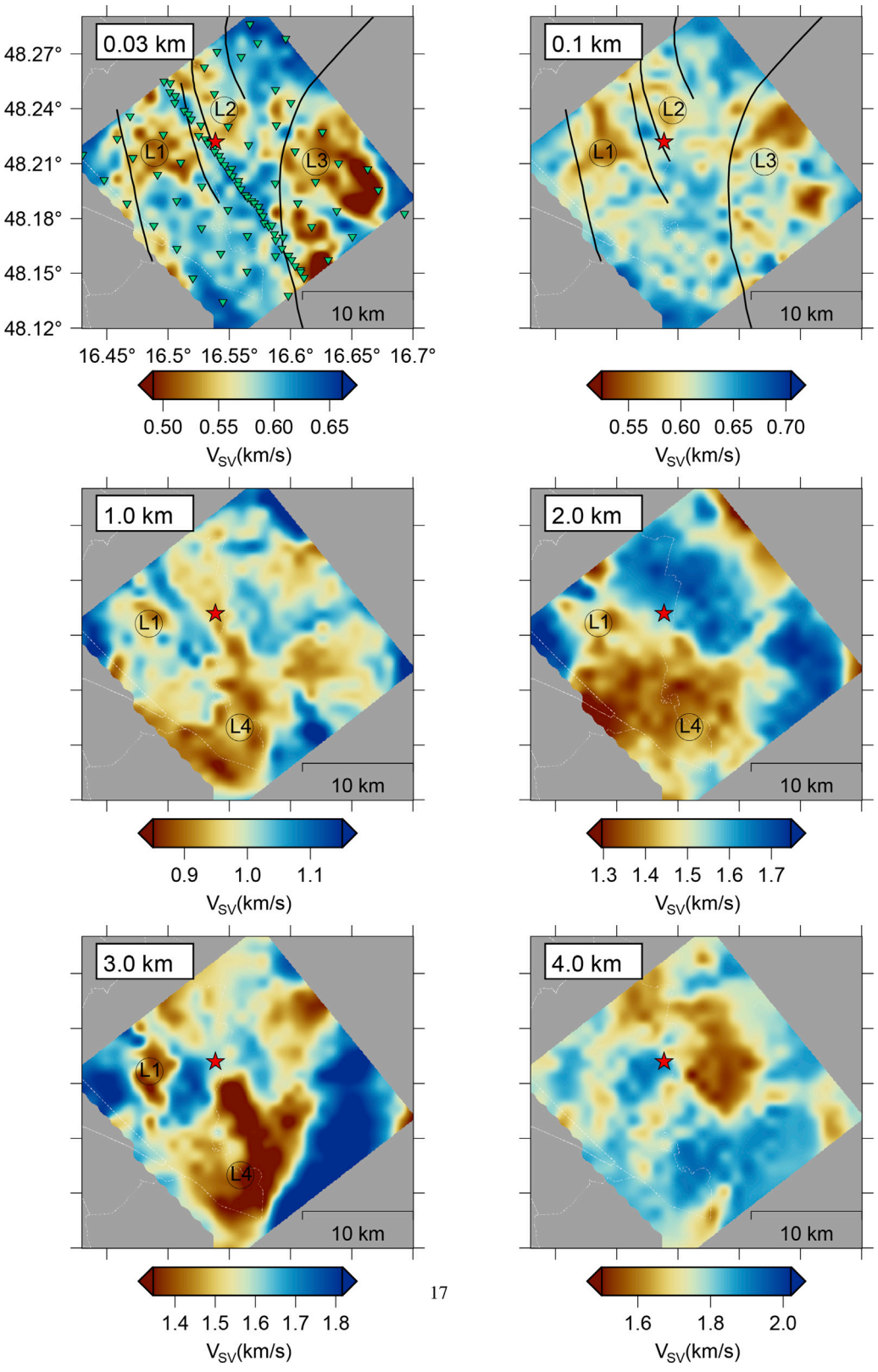

Fig. 5. Depth slices through the 3-D V_{S_V} at depths of 0.03, 0.1, 1.0, 2.0, 3.0, 4.0 km. White dashed-lines show the limit of the city of Vienna. Note that the color scale differs and therefore mean velocity between maps. Inverted green triangles represent nodal seismic stations. Black solid lines represent tectonic faults. (For interpretation of the references to color in this figure legend, the reader is referred to the web version of this article.)

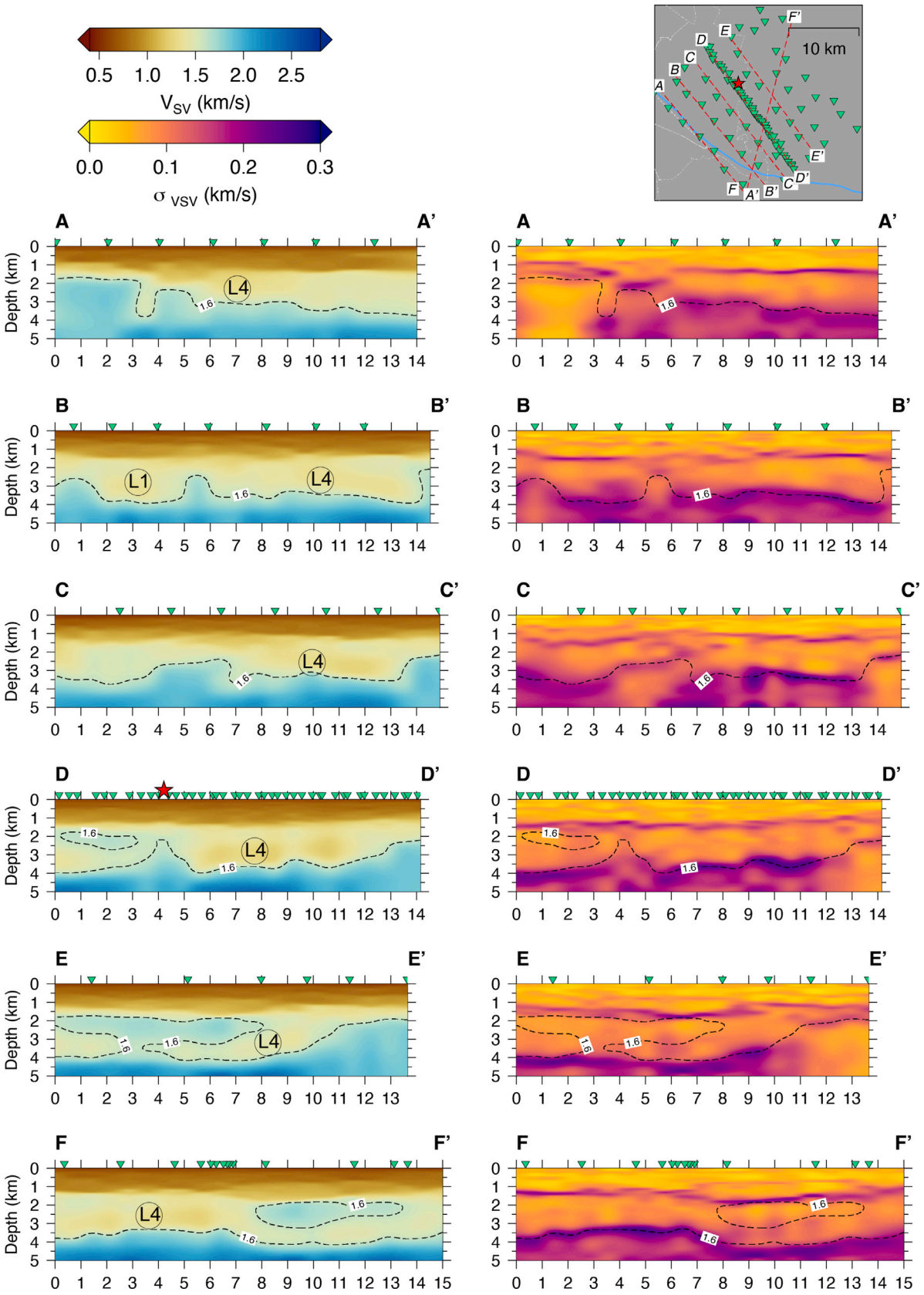

Fig. 6. Profiles through the 3D V_{S_V} model. (Left) Profiles through the 3D V_{S_V} model. The black dashed line shows the iso-velocity contour V_{S_V} = 1.6 km/s. (Right) Same profiles, but showing the V_{S_V} uncertainty. Green inverted triangles show seismic station locations. Red star shows the deep geothermal well *Geotief1*. Refer to the inset map for profile locations. (For interpretation of the references to color in this figure legend, the reader is referred to the web version of this article.)

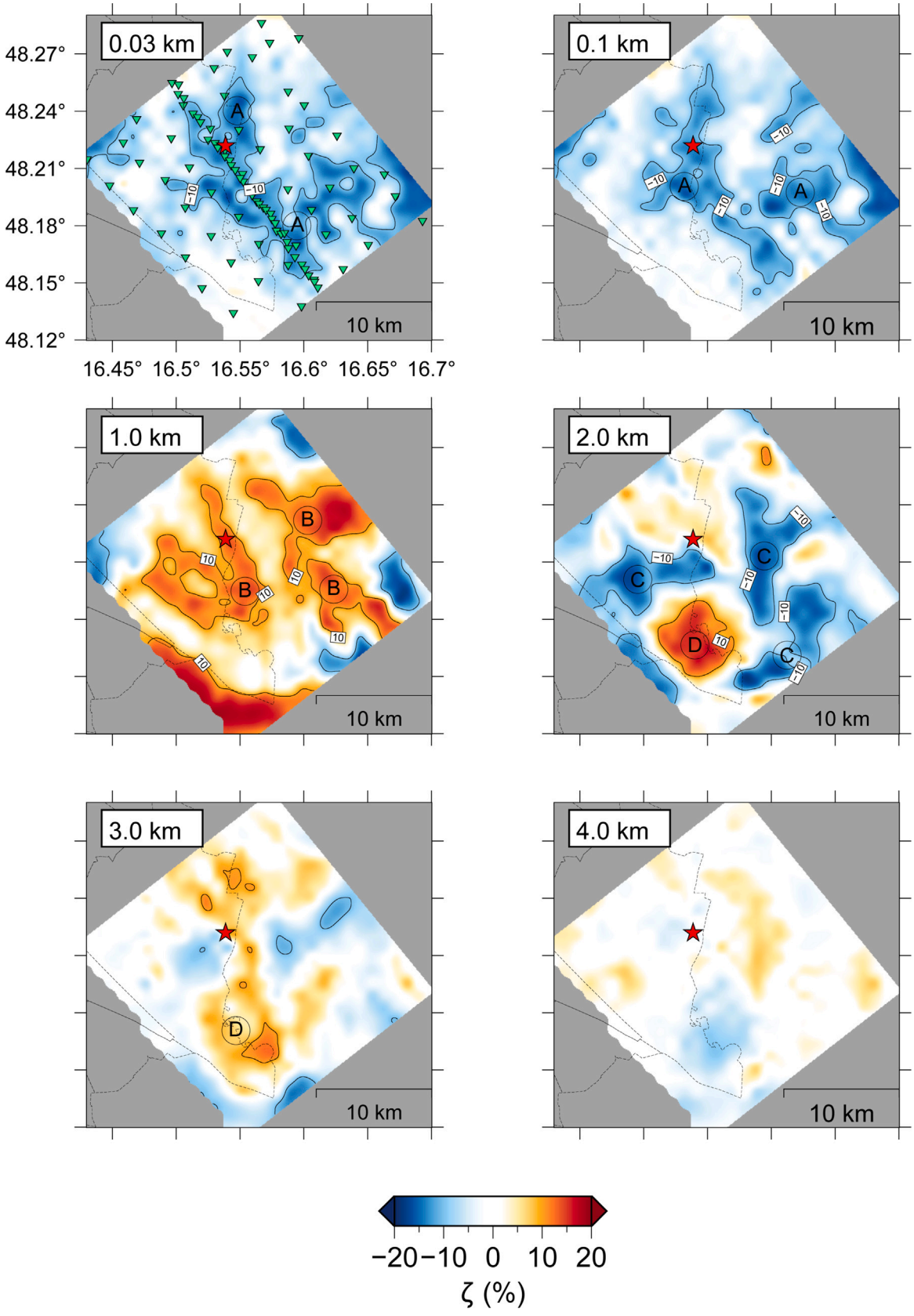

Fig. 7. Shear-wave radial anisotropy at depths of 0.03, 0.1, 1.0, 2.0, 3.0, 4.0 km. Black dashed-lines show the limit of the city of Vienna. Inverted green triangles show station locations. (For interpretation of the references to color in this figure legend, the reader is referred to the web version of this article.)

listric normal faults. The Holocene activity of synthetic sidewall faults is evidenced by faulted sediments (Chwatal et al., 2005), although historical seismicity remains low (Grünthal et al., 2009). Our V_{S_V} model reveals a third low-velocity feature underlying eastern Vienna, which has never been observed before. We speculate that this low-velocity feature might correspond to another Pleistocene sub-basin.

Our 2D Love wave group velocity maps reveal a strong lateral velocity contrast across the MF (Fig. 3, a-b). Similarly, our V_{S_V} model indicates a significant V_{S_V} contrast directly beneath the surface expression of the MF between the surface and 100 m depth, although this contrast is not as pronounced as in the 2D group velocity maps. The depth extent of this lateral V_{S_V} contrast does not exceed 100 m, even though interpreted reflection seismic lines show that the MF extends throughout the entire Neogene basin Beidinger et al. (2011). Salcher et al. (2012) show the variation in sediment thickness from the Top Middle Miocene (11.5 Ma) to present across the fault, noting a 150 m difference in sediment thickness across the MF (see Figure 10 in Salcher et al., 2012), which aligns with the depth extent of the velocity contrast. Thus, we can indirectly observe the MF through the variation in sediment thickness across the fault zone.

5.2. The seismic signature of the schwechat depression

Our V_{S_V} model reveals a low-velocity zone between 1 km and 4 km depth (labeled L4). At 1 km depth, this low-velocity zone is located beneath the southeasternmost part of Vienna (Fig. 5). As the depth increases to between 2.5 and 3 km, the zone extends in a northeast-southwest direction. Beyond 3 km depth, this low-velocity zone shifts eastward and is no longer present beneath the city of Vienna (Fig. 5). In cross-section and 3D views, we see a basin-shaped low-velocity feature, as shown by the southeastward deepening of the iso-velocity surface (V_{S_V} = 1.6 km/s) on profiles AA', BB', CC' and DD' (Fig. 6). The 1.6 km/s V_{S_V} iso-velocity surface is located at a depth where significant uncertainties in V_{S_V} are observed. These large uncertainties likely indicate a vertical velocity contrast, which may represent different lithologies. Thus, we interpret the 1.6 km/s V_{S_V} iso-velocity surface as an indicator of the base of the Neogene basin in the central Vienna Basin. Seismic tomography models reveal the seismic velocity structure in three dimensions; however, so far, we have only examined the structure in 2-D depth slices or vertical cross sections. Fig. 9 presents the 3-D views of the 1.6 km/s V_{S_V} iso-velocity surface and the iso-anisotropy surfaces ($\zeta < -10\%$ and $\zeta > 10\%$), helping the reader to better visualize the structure in three dimensions.

Notably, this low-velocity feature (labeled L4) coincides with the deepest part of the Neogene basin within the central Vienna Basin, the Schwechat depression. We also note that the 1.6 km/s V_{S_V} iso-velocity surface shows important depth variations, reflecting steep edges of the Schwechat depression (Fig. 9a and d). Surrounding this low-velocity anomaly are high-velocity anomalies on both sides. We interpret the low-velocity anomaly to reflect the Neogene basin sediments within the Schwechat depression, while the high-velocity anomalies are associated with the carbonate sedimentary rocks in the Pre-Neogene basement, comprising limestones and dolomites (Fig. 1).

Our V_{S_V} model also shows another small-scale basin-like structure (labeled L1) beneath the eastern part of the city of Vienna, as highlighted by the 1.6 km/s velocity contour (Figs. 5 and 6; profile BB'). This feature extends to an approximate depth of 4 km and appears to be disconnected from the Schwechat depression (Figs. 5, 6 and 9).

5.3. Radial anisotropy beneath the central vienna basin

The top 150 m beneath the surface is characterized by a widespread negative radial anisotropy (labeled A), reflecting a dominant sub-vertical fabric (Figs. 6 and 8). This vertical fabric is most likely caused by nearly vertical cracks or fluid-saturated cracks in the alluvial sediments (Almqvist and Mainprice, 2017). This is in agreement with other sedimentary basins around the world (Kanto Basin, Japan; Tehran Basin, Iran; Jiang and Denolle, 2022; Naghavi et al., 2019), where negative radial anisotropy in the top 300 m of the basin is interpreted to be caused by open and fluid-saturated cracks.

We observe a positive radial anisotropy (labeled B) at depths ranging between 0.15 km and 1.20 km throughout most of the study area (Figs. 7 and 8). Such radial anisotropy contrast is also observed in the Valhall Oil Field in the North Sea (Tomar et al., 2016) or in the Kanto basin Jiang and Denolle (2022) and the positive radial anisotropy is interpreted to reflect the sub-horizontal layering of sedimentary strata. Reflection seismic lines north of our study area also show that the sedimentary layers are sub-horizontal in the Neogene basin Beidinger et al. (2011).

With increasing depth, we note the presence of a negative radial anisotropy (labeled C) and a positive radial anisotropy (labeled D). Along profiles BB', CC' and DD', the negative radial anisotropy (labeled C) encompasses the positive radial anisotropy (labeled D, $\zeta > 10\%$) at depths of 1.5 to 3 km (Fig. 8). We also observe that the negative radial anisotropy (labeled C) occurs where the 1.6 km/s V_{S_V} iso-velocity surface shows significant depth variations (Fig. 8, 9d). This observation is in agreement with (Schreilechner et al., 2022), where they show a structural model derived from a 3D seismic survey in the vicinity of the deep geothermal well *Geotief1*. Their model and a NW-SE interpreted seismic reflection line show a heavily-faulted subsurface and significant variations in the Alpine basement topography (see Figures 5 and 9 in, Schreilechner et al., 2022). Interestingly, the positive radial anisotropy anomaly (labeled D) occurs where the Neogene basin is the thickest, within the Schwechat depression (Fig. 9c). Thus, we suggest that the positive radial anisotropy (labeled D) is controlled by the sub-horizontal sedimentary layering within the Schwechat depression, while the negative radial anisotropy (labeled C) corresponds to the steep dipping layers forming the edges of the Schwechat depression.

5.4. Implications for geothermal exploration in the central vienna basin

The Schwechat depression is the main target for geothermal exploration/production near Vienna for district heating, Recently, Keglovic (2023) showed the lateral temperature variations across the central Vienna Basin at depths corresponding to the top of the Aderklaa formation (inferred from the 3D seismic). Interestingly, we note that the two low-velocity features observed in our V_{S_V} model, labeled L1 and L4, are located in an area with high temperatures exceeding > 100°C beneath Vienna (Keglovic, 2023). Moreover, the positive radial anisotropy model labeled D, interpreted to reflect sub-horizontal layering in the Neogene basin, is co-located with the V_{S_V} anomaly labeled L4. Hamada and Joseph (2020) showed the dependence of V_{S_V} with permeability and porosity. Their results suggest that the slower the V_{S_V}, the higher the permeability and/or porosity, but these correlations remain less clear than V_P. Nonetheless, these seismological evidence tend to suggest that the sedimentary rocks in these regions possess high permeability and porosity, making them ideal for the circulation and storage of geothermal fluids. This confirms that the Schwechat depression is a crucial area for geothermal energy extraction.

Ambient noise tomography obtained from the recordings of dense seismic nodal networks has proven to be an environment-friendly and cost-effective method for geothermal exploration. Such method is needed for improving our understanding of the subsurface and for helping reduce drilling uncertainty. While ambient noise tomography cannot replace active seismic surveys, it can be used to identify specific areas where active seismic campaigns can eventually be conducted for more detailed imaging of the subsurface. It can also be used to spatially extend existing seismic blocks into regions that are not accessible to conventional seismic imaging methods, such as near populated urban centers.

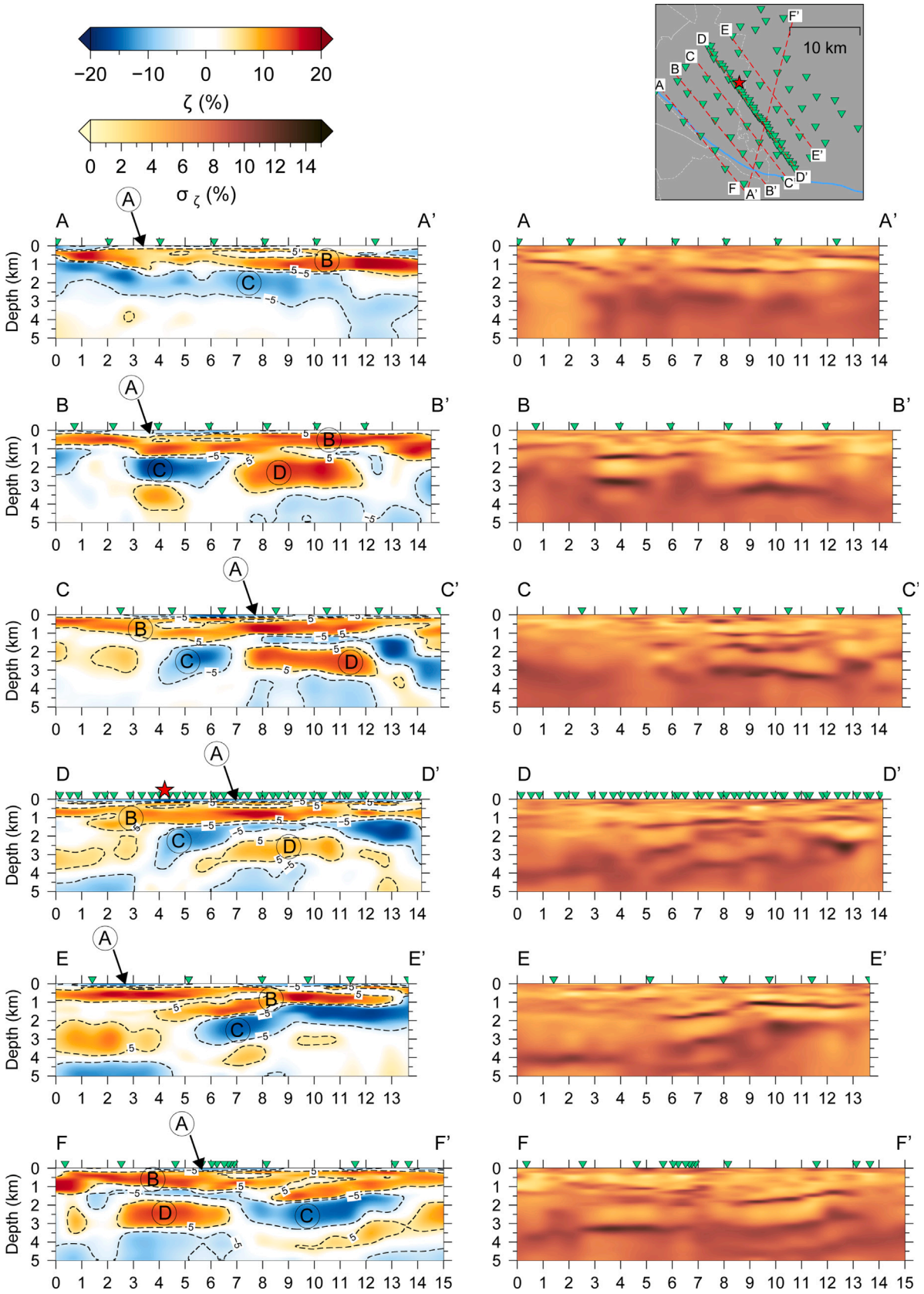

Fig. 8. Profiles through the shear-wave radial anisotropy model (left) and associated uncertainties (right). Format is the same as Fig. 6. (For interpretation of the references to color in this figure legend, the reader is referred to the web version of this article.)

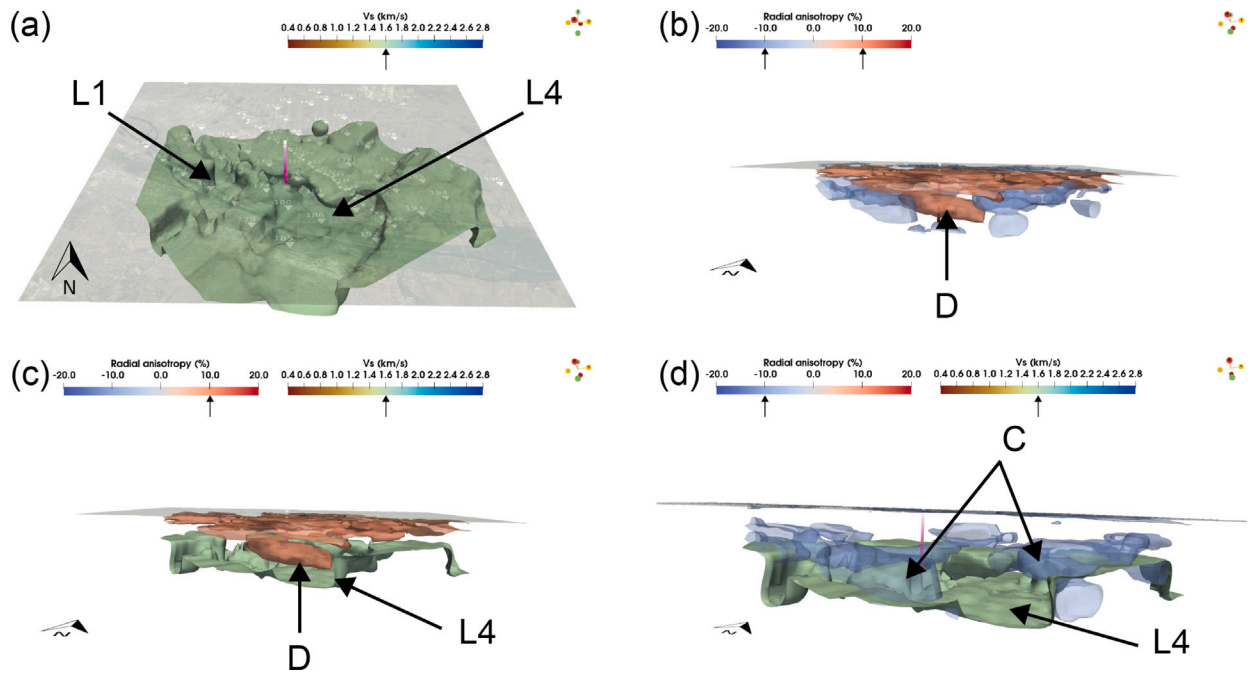

Fig. 9. 3D views of the V_{S_V} and radial anisotropy models. (a) 3D contour plot of the iso-velocity surface V_{S_V} = 1.6 km/s through our V_{S_V} model. (b) 3D contour plot of the iso-anisotropy surfaces $\zeta < -10\%$ and $\zeta > 10\%$ through our radial anisotropy model in blue and orange, respectively. (c) 3D contour plot of the iso-velocity surface V_{S_V} = 1.6 km/s and the iso-anisotropy surface $\zeta > 10\%$. (d) 3D contour plot of the iso-velocity surface V_{S_V} = 1.6 km/s and the iso-anisotropy surface $\zeta < -10\%$. The purple vertical line shows the approximate location of *Geotief1*. (For interpretation of the references to color in this figure legend, the reader is referred to the web version of this article.)

6. Conclusion

We successfully deployed a nodal seismic network in and around the city of Vienna, Austria. The nodal instruments recorded for 5 weeks during summer 2023. We analyze and process the seismic ambient noise recordings, and calculate dispersion curves for all station pairs. We employ a transdimensional approach to calculate 2-D Rayleigh and Love group velocity maps for periods ranging between 0.8 and 5.5 s. Then, we jointly invert Love and Rayleigh dispersion curves to retrieve a 3D V_{S_V} and radial anisotropy model of the central Vienna Basin. Our V_{S_V} model reveals three low-velocity features within the top ~100 m, matching the lateral and depth extent of Pleistocene sedimentary sub-basins. At greater depths, two basin-shaped low-velocity regions are identified in our V_{S_V} model. The largest one correspond to the Schwechat depression, a major depocenter in the central Vienna basin (consisting of up to 4 km of Neogene sediments). The smaller basin-shaped low-velocity region underlies the eastern part of the city of Vienna, and may correspond to another sub-basin.

Our shear-wave radial anisotropy model reveals a complex anisotropic structure in the central Vienna Basin. The top 150 m is characterized by a negative radial anisotropy, which we interpret to be caused by water-saturated open cracks in the near-surface. Then, between 150 m and 1.5 km depth, radial anisotropy is positive, reflecting the sub-horizontal layering of the Neogene basin. The Schwechat depression is characterized by a strong positive radial anisotropy, implying horizontal layering, while the edges of the depression, marked by abrupt and steep dipping strata, are marked by a negative radial anisotropy.

CRediT authorship contribution statement

C. Esteve: Writing – review & editing, Writing – original draft, Visualization, Validation, Software, Methodology, Investigation, Formal analysis, Data curation, Conceptualization. **Y. Lu:** Conceptualization, Data curation, Formal analysis, Investigation, Methodology, Software, Validation, Writing – original draft, Writing – review & editing. **J.M. Gosselin:** Conceptualization, Formal analysis, Investigation, Methodology, Software, Validation, Writing – original draft, Writing – review & editing. **R. Kramer:** Writing – original draft, Writing – review & editing. **Y. Aiman:** Writing – original draft, Writing – review & editing. **G. Bokelmann:** Conceptualization, Supervision, Writing – original draft, Writing – review & editing.

Data statement

The Eastern Vienna Array data set is available upon request.

Open research

The cross-correlation functions, Love and Rayleigh dispersion curves, the 2D Love and Rayleigh group velocity maps, the 3D V_{S_V} model, the shear-wave radial anisotropy model and a *Paraview* file for 3D visualization are available at https://doi.org/10.5281/zenodo.13348597.

Declaration of competing interest

The authors declare that they have no known competing financial interests or personal relationships that could have appeared to influence the work reported in this paper.

Acknowledgments

We thank two anonymous reviewers for their comments and suggestions, which improved the quality of the manuscript. The authors wish to thank Daniel Schützenhofer in assisting all aspects of the field experiment. The authors also thank the city of Vienna, landowners, and *QWS-Bau GmbH* for permitting the deployment of several seismic nodes. Figures were created using *Generic Mapping Tools* (Wessel et al., 2013). Fig. 9 was created using *Paraview* (Ahrens et al., 2005).

Appendix A. Supplementary data

Supplementary material related to this article can be found online at https://doi.org/10.1016/j.geothermics.2024.103211.

Data availability

Data will be made available on request.

References

Ahrens, J., Geveci, B., Law, C., 2005. In: Hansen, C.D., Johnson, C.R. (Eds.), Visualization Handbook. Elsevier Inc., Burlington, MA, USA, pp. 717–731.

Almqvist, B.S.G., Mainprice, D., 2017. Seismic properties and anisotropy of the continental crust: Predictions based on mineral texture and rock microstructure. Rev. Geophys. 55 (2), 367–433. http://dx.doi.org/10.1002/2016RG000552.

Beidinger, A., Decker, K., Roch, K.H., 2011. The Lassee segment of the Vienna basin fault system as a potential source of the earthquake of Carnuntum in the fourth century a.d.. Int. J. Earth Sci. 100 (6), 1315–1329. http://dx.doi.org/10.1007/s00531-010-0546-x.

Bodin, T., Sambridge, M., Rawlinson, N., Arroucau, P., 2012. Transdimensional tomography with unknown data noise. Geophys. J. Int. 189 (3), 1536–1556. http://dx.doi.org/10.1111/j.1365-246X.2012.05414.x.

Calò, M., Di Luccio, F., Persaud, P., Ventura, G., 2023. Ambient noise tomography of the Lipari volcanic island (southern Italy) from a dense nodal array. Geophys. Res. Lett. 50 (4), e2022GL101022. http://dx.doi.org/10.1029/2022GL101022.

Cheng, F., Xia, J., Ajo-Franklin, J.B., Behm, M., Zhou, C., Dai, T., Xi, C., Pang, J., Zhou, C., 2021. High-resolution ambient noise imaging of geothermal reservoir using 3c dense seismic nodal array and ultra-short observation. J. Geophys. Res. Solid Earth 126 (8), e2021JB021827. http://dx.doi.org/10.1029/2021JB021827.

Chwatal, W., Decker, K., Roch, K.H., 2005. Mapping of active capable faults by high-resolution geophysical methods: Examples from the central Vienna basin. Austrian J. Earth Sci. 97, 52–59.

Crampin, S., 1981. A review of wave motion in anisotropic and cracked elastic-media. Wave Motion 3 (4), 343–391. http://dx.doi.org/10.1016/0165-2125(81)90026-3.

Dreiling, J., Tilmann, F., Yuan, X., Giese, J., Rindraharisaona, E.J., Rümpker, G., Wysession, M.E., 2018. Crustal radial anisotropy and linkage to geodynamic processes: A study based on seismic ambient noise in southern Madagascar. J. Geophys. Res. Solid Earth 123 (6), 5130–5146. http://dx.doi.org/10.1029/2017JB015273.

Elster, D., Goldbrunner, J., Wessely, G., Niederbacher, P., Schubert, G., Berka, R., Philippitsch, R., Hörhan, T., 2016. Thermalwässer in Österreich, Geologische Thermenkarte der Republik Österreich. Geologische Bundesanstalt, Vienna, Austria.

Goetzl, G., Faber, R., Janda, C., Schubert, G., Zekiri, F., 2010. Coupled geothermal - hydraulic 3D modeling of the southern vienna basin: A state of the art decision planning tool for sustainable hydrothermal exploitation inside an environment of sensitive hydraulic circulation systems. In: Proceedings World Geothermal Congress 2010. Bali, Indonesia, 25-29 April 2010.

Gosselin, J.M., Audet, P., Schaeffer, A.J., Darbyshire, F.A., Estève, C., 2021. Azimuthal anisotropy in Bayesian surface wave tomography: application to northern Cascadia and Haida Gwaii, British Columbia. Geophys. J. Int. 224 (3), 1724–1741. http://dx.doi.org/10.1093/gji/ggaa561.

Green, P.J., 1995. Reversible jump Markov chain Monte Carlo computation and Bayesian model determination. Biometrika 82 (4), 711–732. http://dx.doi.org/10.1093/biomet/82.4.711.

Green, R.G., Sens-Schönfelder, C., Shapiro, N., Koulakov, I., Tilmann, F., Dreiling, J., Luehr, B., Jakovlev, A., Abkadyrov, I., Droznin, D., Gordeev, E., 2020. Magmatic and sedimentary structure beneath the Klyuchevskoy volcanic group, Kamchatka, from ambient noise tomography. J. Geophys. Res. Solid Earth 125 (3), e2019JB018900. http://dx.doi.org/10.1029/2019JB018900.

Grünthal, G., Wahlström, R., Stromeyer, D., 2009. The unified catalogue of earthquakes in central, northern and northwestern Europe (CENEC)–updated and expanded to the last millennium. J. Seismol. 13, 517–541. http://dx.doi.org/10.1007/s10950-008-9144-9.

Hamada, G., Joseph, V., 2020. Developed correlations between sound wave velocity and porosity, permeability and mechanical properties of sandstone core samples. Petrol. Res. 5 (4), 326–338. http://dx.doi.org/10.1016/j.ptlrs.2020.07.001.

Hawkins, R., Bodin, T., Sambridge, M., Choblet, G., Husson, L., 2019. Trans-dimensional surface reconstruction with different classes of parameterization. Geochem. Geophys. Geosyst. 20 (1), 505–529. http://dx.doi.org/10.1029/2018GC008022.

Hinsch, R., Decker, K., Peresson, H., 2005. 3-d seismic interpretation and structural modeling in the Vienna basin: implications for Miocene to recent kinematics. Austrian J. Earth Sci. 97, 38–50.

Jiang, C., Denolle, M.A., 2022. Pronounced seismic anisotropy in Kanto sedimentary basin: A case study of using dense arrays, ambient noise seismology, and multi-modal surface-wave imaging. J. Geophys. Res. Solid Earth 127 (8), e2022JB024613. http://dx.doi.org/10.1029/2022JB024613.

Keglovic, P., 2023. Deep geothermal energy for decarbonizing the city of Vienna. In: Geothermie Symposium 2023. Geinberg, Austria.

Lee, E.Y., Wagreich, M., 2017. Polyphase tectonic subsidence evolution of the Vienna basin inferred from quantitative subsidence analysis of the northern and central parts. Int. J. Earth Sci. 106 (2), 687–705. http://dx.doi.org/10.1007/s00531-016-1329-9.

Lehujeur, M., Vergne, J., Schmittbuhl, J., Zigone, D., Le Chenadec, A., EstOF Team, 2018. Reservoir imaging using ambient noise correlation from a dense seismic network. J. Geophys. Rese. Solid Earth 123 (8), 6671–6686. http://dx.doi.org/10.1029/2018JB015440.

Lu, Y., Stehly, L., Paul, A., AlpArray Working Group, 2018. High-resolution surface wave tomography of the European crust and uppermost mantle from ambient seismic noise. Geophys. J. Int. 214 (2), 1136–1150. http://dx.doi.org/10.1093/gji/ggy188.

Mainprice, D., Nicolas, A., 1989. Development of shape and lattice preferred orientations: application to the seismic anisotropy of the lower crust. J. Struct. Geol. 11 (1), 175–189. http://dx.doi.org/10.1016/0191-8141(89)90042-4.

Naghavi, M., Hatami, M., Shirzad, T., Rahimi, H., 2019. Radial anisotropy in the upper crust beneath the Tehran basin and surrounding regions. Pure Appl. Geophys. 176 (2), 787–800. http://dx.doi.org/10.1007/s00024-018-1986-7.

Planès, T., Obermann, A., Antunes, V., Lupi, M., 2019. Ambient-noise tomography of the greater Geneva basin in a geothermal exploration context. Geophys. J. Int. 220 (1), 370–383. http://dx.doi.org/10.1093/gji/ggz457.

Rupprecht, B.J., Sachsenhofer, R.F., Zach, C., Bechtel, A., Gratzer, R., Kucher, F., 2018. Oil and gas in the Vienna Basin: hydrocarbon generation and alteration in a classical hydrocarbon province. Petrol. Geosci. 25 (1), 3–29. http://dx.doi.org/10.1144/petgeo2017-056.

Salcher, B.C., Meurers, B., Decker, K., Hölzel, M., Wagreich, M., 2012. Strike-slip tectonics and quaternary basin formation along the Vienna basin fault system inferred from Bouguer gravity derivatives. Tectonics 31 (3), http://dx.doi.org/10.1029/2011TC002979.

Schippkus, S., Zigone, D., Bokelmann, G., the AlpArray Working Group, 2018. Ambient-noise tomography of the wider Vienna basin region. Geophys. J. Int. 215 (1), 102–117. http://dx.doi.org/10.1093/gji/ggy259.

Schreilechner, M.G., Eichkitz, C.G., Binder, H., Hasni, M., Neuhold, C., Jara, C., Jud, M., Schön, J., Wessely, G., Lüschen, E., Sperl, H., Garden, M., Keglovic, P., 2022. Interpretation and modelling for deep geothermal energy in Vienna. First Break 40 (7), 95–99. http://dx.doi.org/10.3997/1365-2397.fb2022062.

Schutt, D.L., Porritt, R.W., Estève, C., Audet, P., Gosselin, J.M., Schaeffer, A.J., Aster, R.C., Freymueller, J.T., Cubley, J.F., 2023. Lithospheric s wave velocity variations beneath the Mackenzie mountains and northern Canadian cordillera. J. Geophys. Res. Solid Earth 128 (1), http://dx.doi.org/10.1029/2022JB025517.

Shapiro, N.M., Singh, S.K., 1999. A systematic error in estimating surface-wave group-velocity dispersion curves and a procedure for its correction. Bull. Seismol. Soc. Am. 89 (4), 1138–1142. http://dx.doi.org/10.1785/BSSA0890041138.

Tomar, G., Shapiro, N.M., Mordret, A., Singh, S.C., Montagner, J.-P., 2016. Radial anisotropy in valhall: ambient noise-based studies of Scholte and Love waves. Geophys. J. Int. 208 (3), 1524–1539. http://dx.doi.org/10.1093/gji/ggw480.

Wessel, P., Smith, W.H.F., Scharroo, R., Luis, J., Wobbe, F., 2013. Generic mapping tools: Improved version released. Eos 94 (45), 409–410. http://dx.doi.org/10.1002/2013EO450001.

Wu, S.-M., Sánchez-Pastor, P., Ágústsdóttir, T., Hersir, G.P., Mordret, A., Hjörleifsdóttir, V., Obermann, A., 2024. Crustal characterization of the Hengill geothermal fields: Insights from isotropic and anisotropic seismic noise imaging using a 500-node array. J. Geophys. Res. Solid Earth 129 (7), e2024JB028915. http://dx.doi.org/10.1029/2024JB028915.